

Understanding high gain twin beam sources using cascaded stimulated emission

Gil Triginer^{*,1}, Mihai D. Vidrighin^{*,1}, Nicolás Quesada^{†,2}, Andreas Eckstein¹,
Merritt Moore¹, W. Steven Kolthammer³, J.E. Sipe⁴ and Ian A. Walmsley^{1,5}

¹*Clarendon Labs, Department of Physics, Oxford University, Parks Road OX1 3PU Oxford*

²*Perimeter Institute for Theoretical Physics, Waterloo, ON, N2L 2Y5, Canada*

³*QOLS, Blackett Laboratory, Imperial College London, London SW7 2AZ, United Kingdom*

⁴*Department of Physics, University of Toronto, Toronto, ON, M5S 1A7, Canada*

⁵*Office of the Provost and Department of Physics,
Imperial College London, South Kensington Campus, SW7 2AZ, UK*

We present a new method for the spectral characterization of pulsed twin beam sources in the high gain regime, using cascaded stimulated emission. We show an implementation of this method for a ppKTP spontaneous parametric down-conversion source generating up to 60 photon pairs per pulse, and demonstrate excellent agreement between our experiments and our theory. This work enables the complete and accurate experimental characterization of high gain effects in parametric down conversion, including self and cross-phase modulation. Moreover, our theory allows the exploration of designs with the goal of improving the specifications of twin beam sources for application in quantum information, computation, sampling, and metrology.

Many pivotal experiments in quantum optics and technology rely on twin beams generated by sources based on parametric nonlinear optical processes, and in recent years there has been significant progress in the development of such sources. In particular, high gain two-mode squeezing in modes with well-defined spatial and spectral properties can be produced by parametric down-conversion (PDC) in waveguiding structures, using quasi-phase-matching and group velocity matching techniques [1–3]. The generation of twin beam pulses with up to tens of photon pairs has been demonstrated experimentally [4]. Together with the development of efficient photon-number-resolving detectors [5], this enables a range of new experiments in quantum optics, such as conditional non-Gaussian state preparation [6, 7] and boson sampling experiments [8–11].

In dispersion-engineered pulsed PDC sources, residual spectral correlations between the down-converted beams, due to effects such as phase-matching revivals and non-uniformity in the spectral phase of pump pulses [12–15], result in the generation of a small number of independently squeezed spectral modes with the same spatial profile. In the high gain regime, self-phase modulation (SPM) of the pump pulses [16] and cross-phase modulation (XPM) induced by the pump on the down-converted beams [17] also affect the spectral structure of PDC emission. In addition, time-ordering corrections to the commonly used perturbative description of PDC must be considered [18, 19]. The complex interplay between all these phenomena makes the study of pulsed PDC sources in the high gain regime challenging, and the development of new techniques for the experimental characterization and theoretical understanding of non-perturbative PDC

a priority. This paper focuses on experimental characterization, while in a companion paper [20] we develop theoretical approaches to treat the non-perturbative regime.

A large body of work has already been devoted to the characterization of PDC sources, of course. Stimulated emission tomography (SET) [21] is a general approach used to infer the quantum properties of a spontaneous nonlinear process, such as spontaneous PDC, from an intensity measurement of its corresponding stimulated process, in this example difference frequency generation (DFG). While it has been the basis of many experiments [22–27], and provides a detailed description of the spectral mode structure of a PDC process, it is generally not used to estimate the degree of squeezing. Although in principle it is possible to derive the squeezing strength from the amount of parametric amplification on a seed beam, in practice this is hindered by uncertainty in the amount of overlap – spatial, spectral, or polarization – between the seeding and amplified modes, as well as by optical loss.

An alternative approach consists in using higher order photon correlation functions of the down-converted field to estimate the number of modes in the source [18, 28, 29]. It has the advantage of being insensitive to loss, but provides little information about the physical mechanisms that degrade the performance of the source.

Here we demonstrate a method that provides detailed spectral information about the generated nonclassical light, and is applicable in the high gain regime. It extends SET to the measurement of all emission processes resulting from a second-order optical nonlinearity. Two parametric amplification processes are seeded simultaneously, with the second seeded by the output of the first (see Figure 1), and so the resulting output intensities scale differently with squeezing strength. The ratio between the output intensities can then be used to estimate squeezing parameters, without any knowledge of detec-

*Equal contributors

†Current affiliation: Xanadu, Toronto, Canada

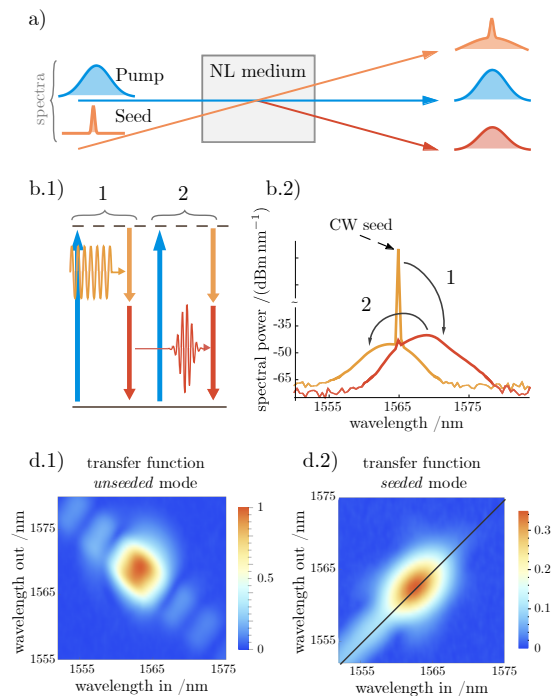


FIG. 1: a) Schematic of an extended SET experiment, including the broadband light generated in the seeding beam through a cascaded DFG process. b.1) Cascaded stimulated emission in a PDC crystal. Seeding one of the two down-conversion modes with a continuous wave (CW) field (represented in orange), bright light is generated through DFG between the pump (represented in blue) and the seed. The DFG signal (represented in red) acts as seed for a second DFG interaction with the pump field, leading to broadband light generation in the mode that was originally seeded. The process is repeated with decreasing strength. b.2) Measured spectra of cascaded stimulated emission for a nearly degenerate type II PDC source pumped with a pulse train centered at 780 nm. Seeding with a CW laser at 1565 nm, we measured broadband signals in the opposite polarization (red) as well as in the same polarization as the seed (orange). c) The full spectral response of the PDC process reconstructed by scanning the seed wavelength. The CW seed contribution was subtracted from the spectra. The spectral responses are normalized to the maximum of the TF corresponding to the unseeded mode.

tion efficiencies or mode overlaps, in a strategy that resembles self-referenced methods for estimating absolute detector efficiency using light generation [30, 31]. Additionally, the output of the second of the processes – cascaded stimulated emission – provides phase information due to the coherent addition of light generated by different pump frequencies, and can be used to estimate the joint spectral phase of the source.

To understand our cascaded stimulated emission measurements, we use simulations of the PDC process, with a small number of parameters extracted from experiments mainly in the low gain regime. We rely on Heisenberg-like equations of motion describing the spatial evolution

of field amplitudes in the PDC source. Within the undepleted classical pump approximation, we introduce an efficient method for solving these equations with arbitrarily high gain. We find excellent agreement between our experiments and our theoretical predictions. We can identify and characterize several effects in the large gain regime that have been difficult to isolate before, including SPM of the pump field and XPM between the pump and the down-converted modes. As our equations describe the PDC source at the quantum level, we are able to accurately quantify the effects of these processes on the generated squeezed vacuum. We also show how to use our experimentally validated simulations to optimize parameters of the source with the goal of improving figures of merit, such as spectral purity. This demonstrates that our approach is fruitful not only for understanding pulsed squeezed light sources, but also for optimizing their design.

The outline of this paper is as follows: In Section I we introduce the spectral transfer functions that can be used to characterize pulsed squeezing, and discuss how they can be extracted from cascaded stimulated emission. Then we give a theoretical framework for calculating parametric down-conversion, valid both in the limits of small and large gain, and discuss how most parameters for our theoretical description are extracted from experiments in the small and large gain limits. We discuss our results, and look forward to future experiments, in Section III. Further technical details are presented in the Appendices.

I. SPECTRAL DESCRIPTION OF PULSED TWIN BEAMS

A. Input-output relations

Assuming negligible propagation losses, and within the undepleted, classical pump approximation, broadband two-mode squeezing in a waveguide source supporting a single spatial mode for each field is fully described by frequency-resolved input-output relations [14, 15, 20]:

$$a_s^{(\text{out})}(\omega) = \int d\omega' U^{s,s}(\omega, \omega') a_s^{(\text{in})}(\omega') + \int d\omega' U^{s,i}(\omega, \omega') a_i^{\dagger(\text{in})}(\omega'), \quad (1a)$$

$$a_i^{(\text{out})}(\omega) = \int d\omega' U^{i,i}(\omega, \omega') a_i^{(\text{in})}(\omega') + \int d\omega' U^{i,s}(\omega, \omega') a_s^{\dagger(\text{in})}(\omega'). \quad (1b)$$

Here $a_{s(i)}^{(\text{in})}(\omega)$ denotes the annihilation operator for the input signal (idler) field at frequency ω , and $a_{s(i)}^{(\text{out})}(\omega)$ denotes the annihilation operator for the respective output

mode. The integrals run over the relevant bandwidths. Both input and output operators satisfy the canonical commutation relations $[a_x(\omega), a_y^\dagger(\omega')] = \delta_{x,y}\delta(\omega-\omega')$ and $[a_x(\omega), a_y(\omega')] = 0$ with $x, y \in \{s, i\}$. The assumptions made in order to derive these relations are detailed in our companion paper [20].

The transfer functions (TFs) $U^{s,s}, U^{s,i}, U^{i,s}$, and $U^{i,i}$ completely describe the spectral properties of the state generated in the PDC process, and all observable quantities, such as correlation functions, can be predicted using Equation (1). The cross-mode TFs $U^{s,i(i,s)}$ are sufficient for describing spontaneous PDC, giving the joint spectral amplitude of a photon pair in the low squeezing regime. However, in this work, we show that measuring the same-mode TFs $U^{s,s(i,i)}$, which are only accessible in the stimulated regime, provides a redundancy that is very useful for studying experiments involving high pump powers, where new effects such as SPM of the pump come into play. In the application presented here, a full set of measurements involving all the TFs is crucial for providing an explanation of the experimental results at high pump powers.

B. Extracting spectral transfer functions from cascaded stimulated emission

In SET measurements, a monochromatic seed field is coupled to one of the two polarization-orthogonal down-conversion spatial modes. In the presence of the pump, this seed generates light in the other mode by parametric amplification, in a process known as DFG. The emission is mapped over a range of seed frequencies, resulting in a joint spectral distribution [21]. This has previously been used to measure the joint spectral intensity of photon pair emission in the low squeezing regime [22].

We can now describe SET using the notation introduced above. Equation (1) remains valid when the annihilation and creation operators are replaced by classical field amplitudes $\alpha_{s(i)}(\omega)$ and their conjugates, as we detail in Appendix A. Therefore, if the idler mode is seeded with the coherent amplitude $\alpha_i^{\text{in}}(\omega)$, light will be generated in the signal mode with the amplitude

$$\alpha_s^{(\text{out})}(\omega) = \int d\omega' U^{s,i}(\omega, \omega') \alpha_i^{*(\text{in})}(\omega'). \quad (2)$$

For large α_i^{in} , the coherent component at the output dominates spontaneous emission, and the measured power spectral density (PSD) in the signal mode is $|\alpha_s^{(\text{out})}(\omega)|^2$, with units of photon number per Hertz. In Appendix B we show that, for low PDC gains, the amplitude of $U^{s,i(i,s)}$ scales linearly with a parametric gain proportional to the pump amplitude, as well as to the crystal nonlinearity.

We can retrieve the absolute value of this transfer function using a narrowband seed at frequency ω_0 , such that the PSD at the output is proportional to $|U^{s,i}(\omega, \omega_0)|^2$.

The proportionality constant is given by the seed intensity, the detection efficiency, and the overlap between the seed mode and the seeded down-conversion mode. Stacking the output spectra measured for a range of seed frequencies, a two-dimensional distribution proportional to $|U^{s,i}(\omega, \omega')|^2$ can be obtained.

According to the classical equivalent of Equation (1), in the seeded measurement, light is also generated in the same mode as the seed, with amplitude

$$\alpha_i^{(\text{out})}(\omega) = \int d\omega' U^{i,i}(\omega, \omega') \alpha_i^{(\text{in})}(\omega'). \quad (3)$$

For low gain (see [13] and Appendix B), $U^{i,i}(\omega, \omega') \approx \delta(\omega - \omega')$, and Equation (3) describes linear propagation, without frequency generation in the seed mode. With a more intense pump field, the squeezing strength increases, and a broadband ‘‘pedestal’’ is generated at frequencies around the seed frequency. In Appendix B we show that, in a series expansion of the TFs up to second order in the PDC interaction strength, the broadband contribution to the same-mode TF arises with the term proportional to the square of the parametric gain. A simple physical picture to understand the broadband pedestal is that of cascaded stimulated emission. The DFG field generated in the signal mode leads to the generation of a new DFG field in the idler mode (see Figure 1).

In a manner analogous to the cross-mode transfer function reconstruction, a two-dimensional distribution proportional to $|U^{i,i}|^2$ can be obtained by measuring the spectral intensity in the idler mode for a range of idler seed frequencies. The two remaining transfer functions are obtained by scanning a narrowband seed in the signal mode and measuring the spectral intensities in the idler ($|U^{i,s}|^2$) and signal ($|U^{s,s}|^2$) modes. We denote the broadband part of a same-mode TF $U_{(b)}^{i,i(s,s)}(\omega, \omega') = U^{i,i(s,s)}(\omega, \omega') - \delta(\omega - \omega')$. To obtain this, we subtract the seed spectrum, which we measure in the absence of the PDC pump, from the output.

These seeded measurements are impacted by the (in general uncalibrated) coupling efficiency of the seed to the down-conversion mode, $\eta_{\text{in}, s(i)}$, as well as by the detection efficiency of the generated outputs, $\eta_{\text{out}, s(i)}$. The stimulated emission from x to y where $x, y \in \{s, i\}$ is given by

$$\eta_{\text{in}, x} \eta_{\text{out}, y} \left| U_{(b)}^{y,x} \right|^2, \quad (4)$$

which hinders the retrieval of the absolute magnitude of the TFs, and therefore the inference of the parametric gain corresponding to the generated twin-beams. We rely on the different scaling of the same and cross-mode TFs with the parametric gain in order to extract it. We define a ratio of TF maxima,

$$\kappa = \frac{\max[|U_{(b)}^{s,s}(\omega, \omega')|] \max[|U_{(b)}^{i,i}(\omega, \omega')|]}{\max[|U^{s,i}(\omega, \omega')|] \max[|U^{i,s}(\omega, \omega')|]}, \quad (5)$$

which can be obtained by replacing the TFs by the respective measured stimulated PSDs, as the η_{in} and η_{out} coefficients defined in equation 4 cancel out. As we have indicated previously, for low PDC gains, the amplitude of the broadband part of the same-mode TFs grows quadratically with the nonlinear gain, while the amplitude of the cross-mode TFs grows linearly: therefore the ratio κ grows linearly with the parametric gain (in the low gain). As we will detail in subsequent sections, this different scaling allows us to obtain the PDC gain from κ , independently of the seeding and detection efficiencies, $\eta_{\text{in}, s(i)}$ and $\eta_{\text{out}, s(i)}$.

C. Theory of parametric down-conversion

We limit our theoretical treatment to waveguide sources with a single transverse spatial mode for each of the signal, idler, and pump fields. The spectral structure of PDC in such a scenario has been studied before in the perturbative [32] and non-perturbative [13–15, 19, 33] regimes. We follow an approach close to that of Wasilewski and Lvovsky [13, 14], describing the evolution of fields in space rather than in time. At high pump powers, one expects that SPM on the pump and XPM induced by the pump on the signal and idler must be considered, and indeed we find these effects significant in our KTP source. In our companion paper [20] we provide a derivation of the equations of motion (EOMs) of the signal and idler annihilation operators, with these effects included. In a medium where group velocity dispersion can be ignored within the bandwidth of the signal and idler modes, it is convenient to use a frame of reference that propagates at the group velocity of the pump beam [20, 34]. Assuming lossless propagation and an undepleted classical pump, the monochromatic annihilation operators for the slowly-varying envelopes of the signal(idler) in this propagating frame of reference, $a_{s(i)}(z, \omega)$, fulfill the following EOMs [20, 34]:

$$\begin{aligned} \partial_z a_s(z, \omega) &= i \Delta k_s(\omega) a_s(z, \omega) \\ &+ i \gamma_{\text{PDC}} g(z) (2\pi)^{-1/2} \int d\omega' \beta_p(z, \omega + \omega') a_i^\dagger(z, \omega') \\ &+ i \gamma_{\text{XPM}, s} (2\pi)^{-1} \int d\omega' \mathcal{E}_p(\omega - \omega') a_s(z, \omega'), \end{aligned} \quad (6a)$$

$$\begin{aligned} \partial_z a_i(z, \omega) &= i \Delta k_i(\omega) a_i(z, \omega) \\ &+ i \gamma_{\text{PDC}} g(z) (2\pi)^{-1/2} \int d\omega' \beta_p(z, \omega + \omega') a_s^\dagger(z, \omega') \\ &+ i \gamma_{\text{XPM}, i} (2\pi)^{-1} \int d\omega' \mathcal{E}_p(\omega - \omega') a_i(z, \omega'). \end{aligned} \quad (6b)$$

The first term on the right hand side of the EOMs contains $\Delta k_{s(i)}(\omega) = (1/v_{s(i)} - 1/v_p)(\omega - \bar{\omega}_{s(i)})$. Here, $v_{s(i)}$ and v_p are the group velocities of the signal(idler) and pump pulses, respectively and $\bar{\omega}_{s(i)}$ is the central frequency of the signal (idler) mode. This term in the

EOMs effectively describes linear propagation through the waveguide.

The complex function $\beta_p(z, \omega)$ is the pump spectral amplitude in the chosen reference frame, which evolves slowly along z due to SPM inside the nonlinear region [20, 35], according to

$$\partial_z \beta_p(z, \omega) = i \gamma_{\text{SPM}} \int d\omega' \mathcal{E}_p(\omega - \omega') \beta_p(z, \omega'). \quad (7)$$

The pump spectral amplitude satisfies the normalization

$$\int d\omega |\beta_p(z, \omega)|^2 = \mathcal{E}_p(0) = E_p, \quad (8)$$

where E_p is the energy in the pump pulse. Note the difference in units between $\beta_p(z, \omega)$ and the $\alpha_{s(i)}(\omega)$ introduced earlier, near Equation (2,3).

The constant γ_{PDC} in equations (6a,6b) is the second order nonlinear coupling strength, and the function $g(z)$ accounts for the possibility of a sign reversal of this coefficient as is the case in periodically poled crystals. It takes the values 1 or -1 over the length of a periodically poled region, and zero outside the crystal.

The third term describes XPM between the pump and the signal (idler), with $\gamma_{\text{XPM}, s(i)}$ a coupling strength that can be different for the signal and idler. This term also contains the frequency autocorrelation function of the pump spectral amplitude, which in this frame of reference is spatially invariant [20],

$$\mathcal{E}_p(\Delta\omega) = \int d\omega'' \beta_p(z_0, \omega'' - \Delta\omega)^* \beta_p(z_0, \omega''). \quad (9)$$

where z_0 is the input face of the waveguide.

The solutions of the EOMs (6a) and (6b) have a special form, which is related to the fact that the commutation relations are preserved [20]. The TFs can always be written as:

$$U^{s,s}(\omega, \omega') = \sum_l \cosh(r_l) \rho_s^{(l)}(\omega) \tau_s^{(l)}(\omega'), \quad (10a)$$

$$U^{s,i}(\omega, \omega') = \sum_l \sinh(r_l) \rho_s^{(l)}(\omega) [\tau_i^{(l)}(\omega')]^*, \quad (10b)$$

$$U^{i,i}(\omega, \omega') = \sum_l \cosh(r_l) \rho_i^{(l)}(\omega) \tau_i^{(l)}(\omega'), \quad (10c)$$

$$U^{i,s}(\omega, \omega') = \sum_l \sinh(r_l) \rho_i^{(l)}(\omega) [\tau_s^{(l)}(\omega')]^*. \quad (10d)$$

Here, $\rho_{s(i)}^{(l)}$ are normalized signal(idler) output spectral modes, $\tau_{s(i)}^{(l)}$ are the corresponding input modes, and r_l are the corresponding squeezing parameters.

Remarkably, if SPM can be neglected and the PDC nonlinearity is uniform or has a homogeneous periodic poling, the EOMs (6a, 6b) can be efficiently solved by exponentiating the discretized differential operator [20]. Scenarios involving slow spatial variations of either the pump amplitude (through SPM) or the effective nonlinearity in periodically poled crystals require an additional

step. In those situations we split the crystal into a number of sections along the propagation direction, within each of which the pump amplitude can be assumed uniform. The input-output relations are then found by sequentially applying the transformations for all sections. This procedure remains very efficient –for the discretized transformations, it amounts to matrix multiplication–, allowing us to perform parameter sweeps effectively even in the high gain regime.

In treatments of squeezing it is sometimes assumed that one can neglect both the cross-phase modulation of the signal and idler by the pump, and the SPM of the pump itself. We refer to treatments that make this assumption as “ $\chi^{(2)}$ models”. Treatments that, in addition, assume a weak quadratic nonlinearity will be referred to as “perturbative $\chi^{(2)}$ models”. The more general description that our EOMs (6a, 6b) provide goes beyond this. The solutions of the EOMs recover features of PDC that have been introduced before as results of time-ordering corrections [19], including an enhanced squeezing rate as a function of the pump power, and the distortion (frequency broadening) of the Schmidt modes [15, 19, 20]. Moreover, they account for the spectral transformation of the twin-beams caused by SPM and XPM. In consequence, we refer to our description as a “ $\chi^{(2)}/\chi^{(3)}$ model”.

In subsequent sections, we address how all the parameters appearing in the EOMs (6a, 6b,7) can be accurately determined, and we experimentally confirm the predictions of the equations.

D. Extracting physical parameters from experiments

Our experimental demonstration employs a wave-guided ppKTP type II PDC source. The pump pulses with central wavelength of 783 nm and pulse duration of around 1 ps, propagate along the ordinary axis of the crystal (H polarization). They generate a signal field with the central wavelength at 1563 nm in the H polarization, and an idler field at 1569 nm in the V polarization. More details are provided in Appendix C.

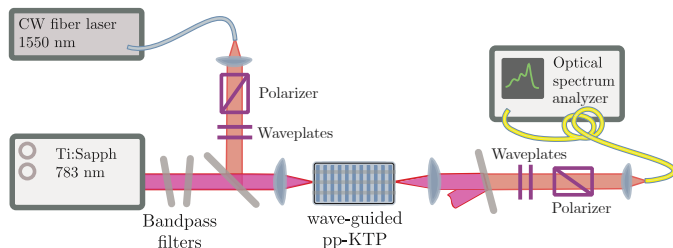


FIG. 2: Experimental setup.

The design, reproduced from earlier work [2], achieves a nearly separable joint spectrum. Therefore, the source generates almost single-mode broadband, orthogonally

polarized twin beams. The waveguide confinement makes the source very bright. Previous to this work, up to 20 photons per pulse (on average) generated by spontaneous PDC has been reported [4]. However, the spectral structure of the twin beams in the high gain regime has not been systematically analysed. Here we show that we can correctly predict the absolute values of the measured TFs for this source up to an inferred mean photon number of 60 per pulse.

The cascaded stimulated emission setup is depicted in Figure 2. We scan the frequency of a CW seed laser across the bandwidth of the signal/idler mode. After selecting a downconverted field by polarization filtering, we record the spectrum of the generated light using an optical spectrum analyzer (OSA). We performed measurements for pump pulse energies ranging from 125 pJ to 600 pJ. For each pump power, we obtained all four TFs (absolute value) as explained in Section I B.

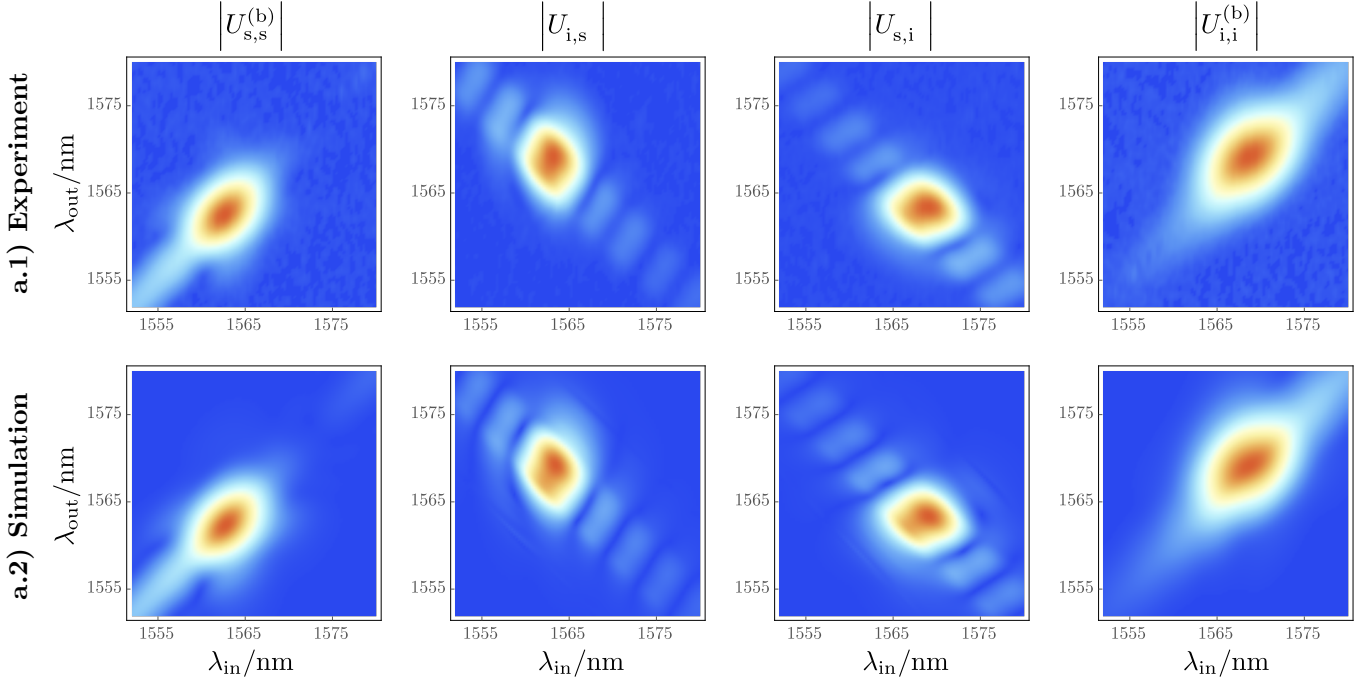
Most parameters in equations 6 can be measured for this source in the low gain regime, either from stimulated emission data or from simple complementary experiments, as we summarize in this section. The values of the parameters, as well as the methods we used to obtain them, are listed in Table I. The reader interested in replicating our method can find the necessary details in Appendix D.

We measure the pump power spectral amplitude, $|\beta_p(z=0, \omega)|^2$ (Appendix D 1) with an optical spectrum analyzer (OSA). We extract the spectral phase of the pump, $\arg(\beta_p(z=0, \omega))$ using a standard ultra-fast spectral phase measurement, SPIDER, for the laser pulse, and a spectral self-interference measurement (Appendix D 2) for the phase added by the bandpass filters used to shape the pump pulse, as shown in Figure 2.

We obtain the group velocity mismatch between pump and signal(idler) pulses, $(1/v_{s(i)} - 1/v_p)$, from the angle and bandwidth of the phase-matching function in a low gain JSI (Appendix D 3). This is confirmed by a direct interferometric measurement of the differential delay between the two polarizations (signal/idler) using a broadband field that propagates through the birefringent ppKTP crystal (Appendix D 3).

We extract the PDC interaction strength, γ_{PDC} , from the ratio between the maxima of the same-mode and cross-mode TFs in the low gain regime, where these amplitudes are not influenced by other nonlinear processes (Appendix D 4). The XPM interaction strength is obtained from the shape of the same-mode TF in the low gain regime alone, as we show in the next section, as well as in Appendix D 5. The SPM interaction strength, γ_{SPM} , is the only parameter that we extract from a fit in the high gain regime: once all other parameters are fixed, γ_{SPM} is chosen to optimize the fitting of the high gain TFs (Appendix D 6).

a) Low squeezing (~ 2 photons/pulse spontaneous emission)



b) High squeezing (~ 60 photons/pulse spontaneous emission)

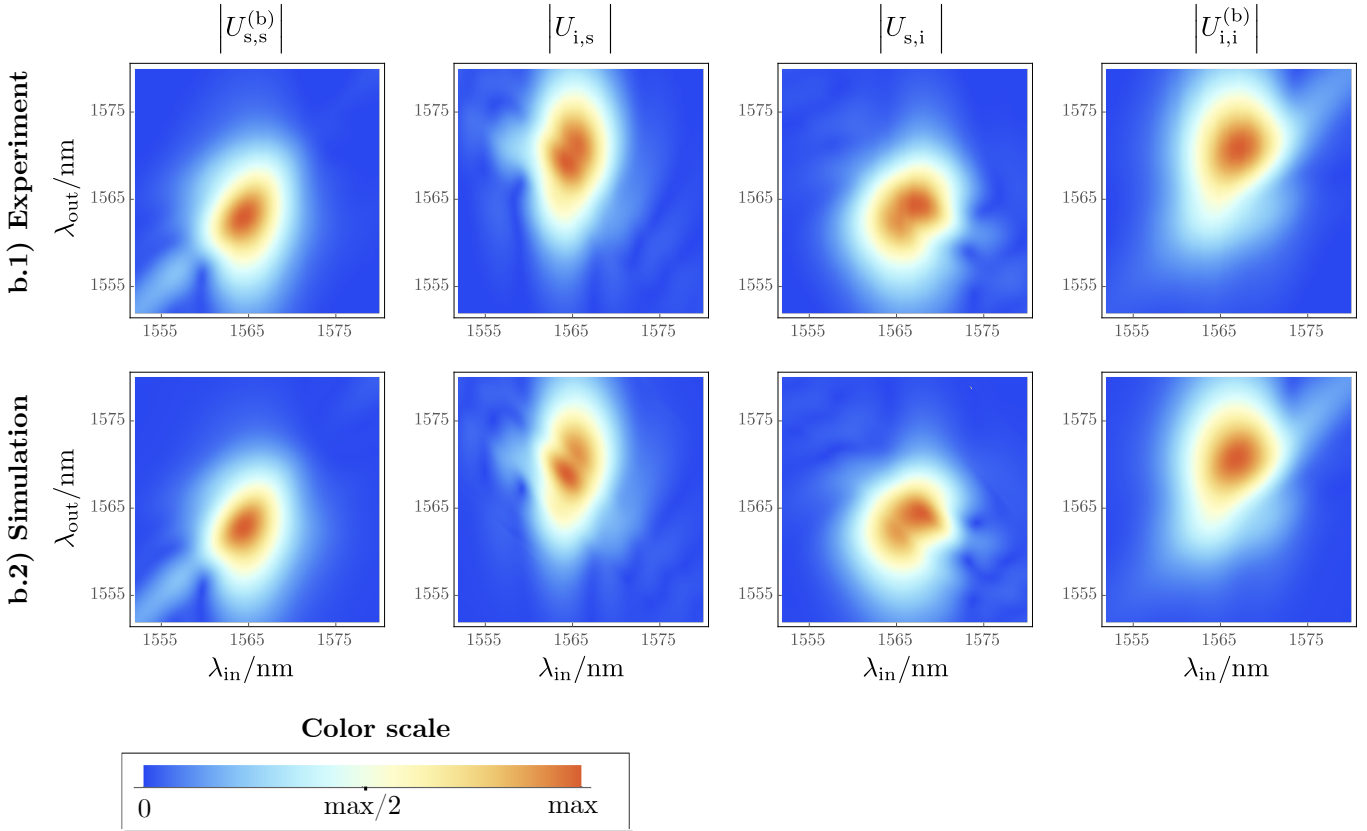


FIG. 3: All measured and modeled TF amplitudes, in the low and high gain regimes, corresponding to strong and weak squeezing. The color scale is normalized separately for each density plot. The TF amplitudes are plotted as a function of wavelength instead of angular frequency, where these are connected by $\lambda = 2\pi c/\omega$.

Parameter	Symbol	Value	Method
Pump spectral amplitude	$ \beta_p(z_0, \omega_p) $	—	Optical spectrum analyzer
Pump spectral phase	$\arg[\beta_p(z_0, \omega_p)]$	—	SPIDER and Spectral interferometry
Group velocity mismatch	$1/v_s - 1/v_p$	1.70 ps/cm	Angle and bandwidth of phase-matching profile + direct interferometric measurement of group delay
	$1/v_i - 1/v_p$	-1.02 ps/cm	
PDC coupling	γ_{PDC}	$28 \text{ W}^{-1/2} \text{ m}^{-1}$	Ratio of the cross-mode and same-mode TF amplitudes
XPM coupling	$\gamma_{\text{XPM,s}}$	$0.16 \text{ W}^{-1} \text{ m}^{-1}$	Asymmetry of the same-mode TFs
	$\gamma_{\text{XPM,i}}$	$0.059 \text{ W}^{-1} \text{ m}^{-1}$	
SPM coupling	γ_{SPM}	$0.56 \text{ W}^{-1} \text{ m}^{-1}$	Fitting of TFs in the high gain regime

TABLE I: Model parameters.

II. EXPERIMENTAL DEMONSTRATION

Here we report our cascaded stimulated emission measurements for an ample range of gains, and demonstrate the excellent agreement with our simulated TFs. Figure 3 summarizes the results for the lowest and highest pump pulse energies. Each measured TF amplitude is compared to the prediction of our EOMs (6a,6b), with parameters fitted as explained in detail in Appendix D. Remarkably, a single model is able to accurately account for all the experimental data. In what follows we report on the most important features of the measured TFs, and provide their physical interpretation.

A. Low gain spectra

We first measured the cross-mode stimulated emission using a relatively low pump power (125 pJ), reproducing a standard SET experiment. The square roots of the resulting 2-dimensional PSDs, corresponding to the absolute value of $U^{s,i}$ and $U^{i,s}$, are depicted in the low gain section of Figure 3. We inferred a spontaneous emission rate of approximately 2 photons/pulse. In this regime, the cross-mode TF is equal to the joint spectral amplitude of the generated photon pairs.

In the same setup, we were able to resolve broadband stimulated emission in the same polarization as the CW seed, centered around the seed wavelength. By scanning the seed wavelength, we reconstructed the two-dimensional spectral distributions, which are shown in the low gain section in Figure 3. As discussed in section IB, these are proportional to the absolute value of the same mode TFs $U_{(b)}^{s,s}$ and $U_{(b)}^{i,i}$.

In Figure 4, we compare experiment and simulation along the $\omega' \equiv \omega_{\text{in}} = \omega_{\text{out}} \equiv \omega$ cut of the same mode TFs. We added for comparison the prediction of a $\chi^{(2)}$ model. The $\chi^{(2)}$ model is significantly less accurate, failing to predict the asymmetry in the tails of the distribution observed experimentally. We found that this asymmetry is explained by the presence of cross-phase modulation induced by the pump pulse on the down-converted modes.

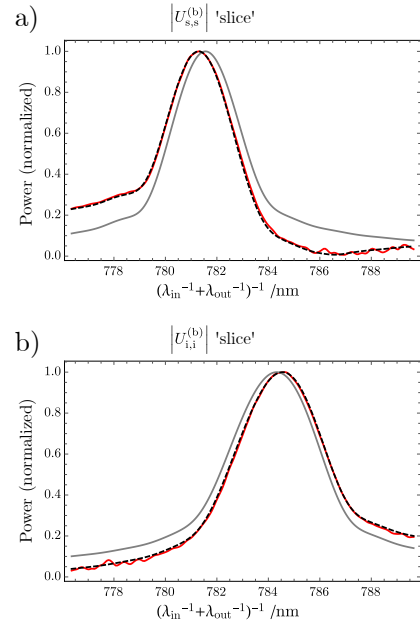


FIG. 4: Same-mode TF slices showing the effect of XPM. The plots show $|U_{(b)}^{s,s(i,i)}(\lambda_{\text{in}}, \lambda_{\text{out}})|$ for $\lambda_{\text{in}} = \lambda_{\text{out}}$. Red: Measurement (background subtracted). Black dashed: model prediction. Gray: prediction of a model that does not include XPM. The asymmetry arises from superposing the signals generated by cascaded stimulated PDC and XPM.

For frequencies far from the PDC phasematching, the effect of XPM appears as a pedestal around the CW seed. Along the $\omega_{\text{in}} = \omega_{\text{out}}$ contour, XPM results in a fixed background. The broadband component of the same-mode PDC TFs, as obtained from our simulations and analytically proven in Appendix B, shows a π phase-jump around the phase-matching central wavelength. As a result, the coherent addition of the constant XPM background and the PDC signal results in an asymmetric shape, reminiscent of a Fano resonance. As indicated above and detailed in Appendix D5, we extracted the XPM interaction strength by optimizing the experiment-theory fit for the profiles in Figure 4. We found that

the XPM interaction strength is not equal for the signal and idler modes, and we analyze this observation in detail in Appendix E. The signal (with the same polarization as the pump) has an XPM interaction strength roughly three times greater than the idler (with polarization orthogonal to that of the pump). The asymmetry of the same-mode TFs is observed to be independent of the pump power, as both cascaded PDC and XPM scale quadratically with the pump amplitude in the low gain regime. This makes it a robust feature, and a good way to estimate the ratio between $\chi^{(2)}$ and $\chi^{(3)}$ interaction strengths.

B. High gain spectra

Increasing the pump power, we observed additional deviations from the $\chi^{(2)}$ model discussed above. The high gain section in Figure 3 shows measurements with a pump pulse energy of 600 pJ; we inferred a spontaneous generation rate of about 60 pairs of photons per pump pulse. As expected in the high gain regime, phase matching lobes are suppressed, and the spectra are broadened [18]. In addition to these effects, accounted for by the $\chi^{(2)}$ model, the cross-mode TFs are highly distorted and the same-mode TFs show a significant asymmetry with respect to the $\omega_{\text{in}} = \omega_{\text{out}}$ line.

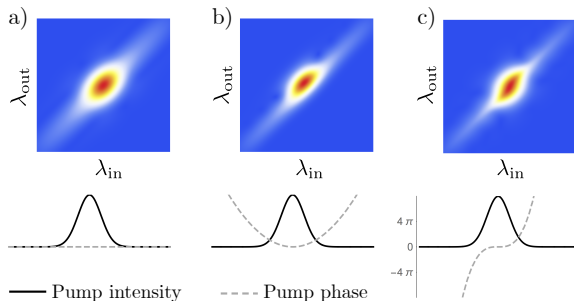


FIG. 5: The amplitudes of the same-mode TFs, $U_{(b)}^{r,s(i,i)}(\omega, \omega')$. Simulated same-mode TF for a) Fourier limited, b) chirped, and c) higher-order chirped Gaussian pump pulses (intensity and bandwidth in arbitrary units). A chirped pump causes a displacement of the same-mode TF from the diagonal (b), while a higher-order chirp leads to a more complicated deformation of the same-mode TF.

We can fully account for these features by including the effect of self-phase modulation of the pump into Equations (6a,6b). The distortion of the cross-mode TFs is related to the broadening and splitting of the pump spectrum through SPM. The shift of the same-mode TFs can be explained by the chirp accumulated by the pump pulse, also due to SPM. As illustrated in Figure 5, the spectral phase of the pump is mapped onto the absolute value of the same-mode TFs, as signals generated by different pump frequencies add up coherently in the cascaded frequency generation process. In particular, a

quadratic phase in the pump field causes a shift of the same-mode TFs away from the $\omega_{\text{in}} = \omega_{\text{out}}$ line. The excellent agreement between this full model and the high gain data is clear evidence that SPM becomes relevant at this pump pulse energy.

C. Scaling and absolute, loss-independent validation

The different scaling of same- and cross-mode TFs gives us access to the twin-beam gain using cascaded stimulated emission measurements outside of the high gain regime. As we show in Section IB and Appendix D 4, we can use ratios of the measured PSDs to construct the coefficient κ , defined in Equation 5, which grows monotonically with the PDC interaction strength, and which is independent of detection efficiency and mode overlap. Note that this coefficient captures features related to the gain of the process in both the low- and high gain regimes, and that in the low gain it gives information pertaining to the squeezing parameters characterizing the transformation of operators in equation (10d). Figure 6 shows that our theory correctly predicts the scaling of κ observed in the experiments.

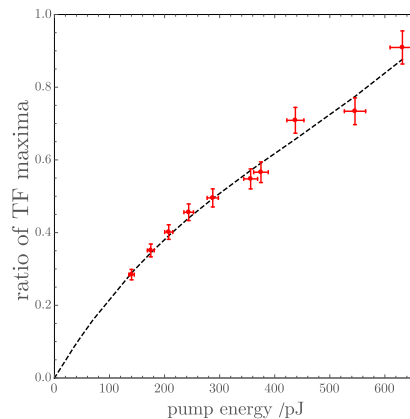


FIG. 6: Ratio between the self and cross-mode transfer functions (κ) for different pump pulse energies.

D. Difference between measurement and simulation

Our theoretical model is consistent with experimental data for a broad range of spontaneous photon pair generation rates, from 1 photon pair/pulse on average to 60 photon pairs/pulse. To quantify the agreement between experiment and theory, we introduce the integrated squared error between the measured and simu-

lated absolute values of the TFs, normalized to unit area:

$$\begin{aligned} \varepsilon^{x,y} &= \int d\omega d\omega' \left| \frac{|U_{\text{meas}}^{x,y}(\omega, \omega')|}{\mathcal{N}_{\text{meas}}^{x,y}} - \frac{|U_{\text{sim}}^{x,y}(\omega, \omega')|}{\mathcal{N}_{\text{sim}}^{x,y}} \right|^2, \\ \mathcal{N}_{\text{sim}}^{x,y} &= \left[\int d\omega d\omega' |U_{\text{meas}}^{x,y}(\omega, \omega')|^2 \right]^{1/2}, \\ \mathcal{N}_{\text{sim}}^{x,y} &= \left[\int d\omega d\omega' |U_{\text{sim}}^{x,y}(\omega, \omega')|^2 \right]^{1/2}, \\ x, y &\in \{s, i\}. \end{aligned} \quad (11)$$

Here, $U_{\text{meas}}^{x,y}(\omega)$ is the broadband part of the power spectral density measured in mode y when seeding mode x , and $U_{\text{sim}}^{x,y}(\omega)$ is the corresponding simulated TF. In Figure 7 we show that, using the calibrated $\chi^{(2)}/\chi^{(3)}$ model (solid lines), $\varepsilon^{x,y} < 2\%$ for all pump powers. On the other hand, neglecting the effect of XPM and SPM (dashed lines) we cannot produce a model that fits the experimental data for all pump powers.

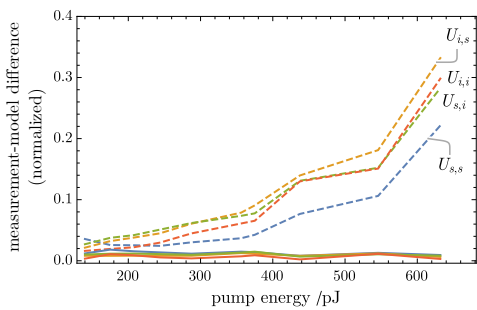


FIG. 7: Mean-squared error between measured and modeled TFs (details in the Methods section). Solid lines – $\chi^{(2)}/\chi^{(3)}$ model; dashed lines – $\chi^{(2)}$ model.

III. PERFORMANCE OF THE SOURCE

We have characterized a source designed to provide a high degree of squeezing in a small number of spectral modes. We have developed a theoretical description that is validated by our experimental results. We now use this description to analyze the performance of the source. In particular, we discuss high gain effects on brightness and spectral purity.

A. Photon number

We can calculate the spontaneously generated mean photon number by adding the squares of the Schmidt coefficients of the cross-mode TF [15], $\langle n \rangle = \sum_l \sinh^2(r_l)$. A perturbative computation of the cross-mode TFs (e.g. Appendix B) yields squeezing parameters linearly proportional to the pump amplitude, and thus a spontaneously generated mean photon number $\langle n \rangle =$

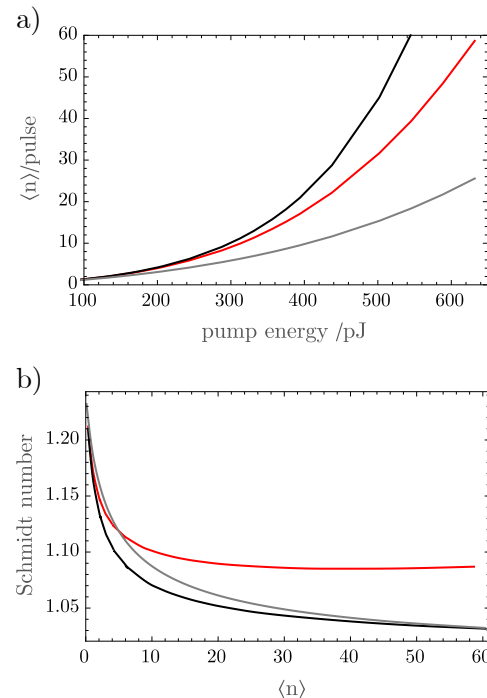


FIG. 8: a) Number of spontaneously generated photons as a function of pump pulse energy. b) Spectral Schmidt number as a function of the number of spontaneously generated photons. Red – the $\chi^{(2)}/\chi^{(3)}$ model; black – a $\chi^{(2)}$ model (only PDC, no SPM or XPM); gray – perturbative $\chi^{(2)}$ model (squeezing parameters $r_l = \sqrt{P} c_l$) with the same predictions in the low gain regime.

$\sum_l \sinh^2(c_l \sqrt{E_p})$, where E_p is the pump pulse energy, and c_l are constants. Our theoretical approach based on integrating EOMs offers revised predictions, previously treated as time-ordering corrections [15, 19]. For $\langle n \rangle > 2$, the squeezing parameters scale nonlinearly with the pump amplitude, leading to an enhanced growth of $\langle n \rangle$. On the other hand, SPM of the pump pulse leads to a lower $\langle n \rangle$ than that predicted by a $\chi^{(2)}$ model. Figure 8.a shows our results: we infer $\langle n \rangle$ from the fitted TFs and find that we are well into the regime where non-perturbative corrections become significant, and that SPM also has a significant effect on the spontaneously generated photon number. Our simulations show that the effect of XPM on the mean photon number is negligible.

B. Spectral purity

We now consider the spectral multimodeness of the source, quantified by the Schmidt number, defined as $K = (\sum_l \sinh(r_l)^2)^2 / (\sum_l \sinh(r_l)^4)$ [18, 36]. A low Schmidt number implies that there is little correlation between the frequency spread of the signal and idler modes, and thus, ultimately, very low spectral entanglement. This situation therefore allows high purity single pho-

tons to be heralded from pairs generated in the low gain regime. More generally, the Schmidt number quantifies the maximum visibility of the second order interference between the generated light and another optical mode [37]. It has been shown that the Schmidt number of a PDC source is reduced in the high gain regime, due to the dominance of strongly populated modes [15, 38]. We found that the pump SPM counteracts this effect: the Schmidt number saturates at a moderate pump power. Figure 8 illustrates these observations. Our simulations show that the effect of XPM on the spectral Schmidt number is negligible.

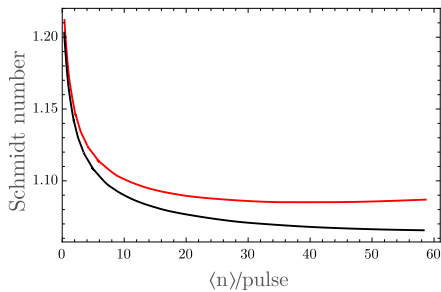


FIG. 9: Effect of pre-chirping pump pulses on the spectral Schmidt number of a PDC source as a function of the average number of photons generated. Red – Fourier-limited pump pulses; black – pre-chirped pump pulses.

C. Improving source performance

We have shown that SPM due to the $\chi^{(3)}$ nonlinearity of KTP has an impact on the performance of our source in the high gain regime. The results of our study, however, suggest a simple optimization to counteract this effect: pre-chirping of the pump pulses. If the sign and magnitude of the chirp are appropriately chosen, it is possible to counter the reduction in purity and brightness. In Figure 9 we show the Schmidt number predicted by our theory as a function of the spontaneously generated photon number, contrasted with what could be achieved using chirped pump pulses. The dispersion parameter

required to optimize the performance of the source is $D = 178$ fs/nm, which can be easily achieved using a grating-based pulse compressor.

IV. CONCLUSIONS

In this work we have demonstrated a general experimental framework to characterize broadband twin-beam sources in the high gain regime. We have introduced cascaded stimulated emission tomography, a seeded measurement which generalizes SET, providing additional spectral information about the generated twin-beams. In particular, we have shown that the redundancy offered by this measurement allows for the self-referenced inference of the PDC interaction strength, independently of seeding and detection efficiency. Using the information offered by cascaded SET, together with a small number of complementary measurements, we have fitted a theoretical model of twin-beam generation, which yields all the complex TFs that describe the process. We have experimentally identified and quantified non-perturbative, SPM, and XPM effects in a high gain PDC source. In fact, the development of the EOMs (6a, 6b, 7) was prompted by features of the data that we were not initially able to explain. Moreover, our ability to modify the parameters of the model has allowed us to identify limitations of the current source design and to explore new designs which overcome these shortcomings. We believe that the framework presented here will move forward the study and design of twin-beam sources in the high gain regime.

Acknowledgements

G.T. thanks Merton College, Oxford, for its support. M.D.V. thanks the Engineering and Physical Sciences Research Council for funding through grant EP/K034480/1 (BLOQS). N.Q. and J.E.S. thank the National Science and Engineering Research Council of Canada.

-
- [1] P.J. Mosley et al. Heralded generation of ultrafast single photons in pure quantum states. *Phys. Rev. Lett.*, 100:133601, Apr 2008.
 - [2] A. Eckstein et al. Highly efficient single-pass source of pulsed single-mode twin beams of light. *Phys. Rev. Lett.*, 106:013603, Jan 2011.
 - [3] Morgan M. Weston, Helen M. Chrzanowski, Sabine Wollmann, Allen Boston, Joseph Ho, Lynden K. Shalm, Varun B. Verma, Michael S. Allman, Sae Woo Nam, Raj B. Patel, Sergei Slussarenko, and Geoff J. Pryde. Efficient and pure femtosecond-pulse-length source of polarization-entangled photons. *Opt. Express*, 24(10):10869–10879, May 2016.
 - [4] G. Harder et al. Single-mode parametric-down-conversion states with 50 photons as a source for mesoscopic quantum optics. *Phys. Rev. Lett.*, 116:143601, 2016.
 - [5] D. Fukuda et al. Titanium-based transition-edge photon number resolving detector with 98% detection efficiency with index-matched small-gap fiber coupling. *Opt. Express*, 19(2):870–875, Jan 2011.
 - [6] A. Zavatta et al. Quantum-to-classical transition with single-photon-added coherent states of light. *Science*, 306(5696):660–662, 2004.

- [7] J. Wenger et al. Non-gaussian statistics from individual pulses of squeezed light. *Phys. Rev. Lett.*, 92:153601, Apr 2004.
- [8] AP Lund, A Laing, S Rahimi-Keshari, T Rudolph, Jeremy L O'Brien, and TC Ralph. Boson sampling from a gaussian state. *Physical Review Letters*, 113(10):100502, 2014.
- [9] Craig S Hamilton, Regina Kruse, Linda Sansoni, Sonja Barkhofen, Christine Silberhorn, and Igor Jex. Gaussian boson sampling. *Physical Review Letters*, 119(17):170501, 2017.
- [10] AP Lund, S Rahimi-Keshari, and TC Ralph. Exact boson sampling using gaussian continuous-variable measurements. *Physical Review A*, 96(2):022301, 2017.
- [11] Joonsuk Huh, Gian Giacomo Guerreschi, Borja Peropadre, Jarrod R McClean, and Alán Aspuru-Guzik. Boson sampling for molecular vibronic spectra. *Nature Photonics*, 9(9):615, 2015.
- [12] C. K. Law, I. A. Walmsley, and J. H. Eberly. Continuous frequency entanglement: Effective finite hilbert space and entropy control. *Phys. Rev. Lett.*, 84:5304–5307, Jun 2000.
- [13] W. Wasilewski et al. Pulsed squeezed light: Simultaneous squeezing of multiple modes. *Phys. Rev. A*, 73:063819, Jun 2006.
- [14] A. I. Lvovsky, Wojciech Wasilewski, and Konrad Banaszek. Decomposing a pulsed optical parametric amplifier into independent squeezers. *Journal of Modern Optics*, 54(5):721–733, 2007.
- [15] A. Christ, B. Brecht, W. Mauerer, and C. Silberhorn. Theory of quantum frequency conversion and type-ii parametric down-conversion in the high-gain regime. *New Journal of Physics*, 15(5):053038, 2013.
- [16] M. L. Sundheimer et al. Large nonlinear phase modulation in quasi-phase-matched ktp waveguides as a result of cascaded second-order processes. *Opt. Lett.*, 18(17):1397–1399, Sep 1993.
- [17] C. Liberale et al. Cross-phase modulation due to a cascade of quadratic interactions in a ppln waveguide. 12:405 – 411, 06 2006.
- [18] A.Christ et al. Probing multimode squeezing with correlation functions. *New Journal of Physics*, 13(3):033027, 2011.
- [19] N. Quesada and J. E. Sipe. Effects of time ordering in quantum nonlinear optics. *Phys. Rev. A*, 90:063840, Dec 2014.
- [20] Nicolás Quesada, Gil Triginer, Mihai D Vidrighin, and JE Sipe. Efficient simulation of high-gain twin-beam generation in waveguides. *arXiv preprint arXiv:1907.01958*, 2019.
- [21] M. Liscidini and J. E. Sipe. Stimulated emission tomography. *Phys. Rev. Lett.*, 111:193602, Nov 2013.
- [22] A. Eckstein et al. High resolution spectral characterization of two photon states via classical measurements. *Laser & Photonics Reviews*, 8(5):L76–L80.
- [23] Bin Fang, Offir Cohen, Marco Liscidini, John E. Sipe, and Virginia O. Lorenz. Fast and highly resolved capture of the joint spectral density of photon pairs. *Optica*, 1(5):281–284, Nov 2014.
- [24] B. Fang, M. Liscidini, J. E. Sipe, and V. O. Lorenz. Multidimensional characterization of an entangled photon-pair source via stimulated emission tomography. *Opt. Express*, 24(9):10013–10019, May 2016.
- [25] Lee A. Rozema, Chao Wang, Dylan H. Mahler, Alex Hayat, Aephraim M. Steinberg, John E. Sipe, and Marco Liscidini. Characterizing an entangled-photon source with classical detectors and measurements. *Optica*, 2(5):430–433, May 2015.
- [26] I. Jizan et al. Phase-sensitive tomography of the joint spectral amplitude of photon pair sources. *Opt. Lett.*, 41(20):4803–4806, Oct 2016.
- [27] V. Ansari et al. Temporal-mode measurement tomography of a quantum pulse gate. *Phys. Rev. A*, 96:063817, Dec 2017.
- [28] E.A. Goldschmidt et al. Mode reconstruction of a light field by multiphoton statistics. *Phys. Rev. A*, 88:013822, Jul 2013.
- [29] I.A Burenkov et al. Full statistical mode reconstruction of a light field via a photon-number-resolved measurement. *Phys. Rev. A*, 95:053806, May 2017.
- [30] D N Klyshko. Use of two-photon light for absolute calibration of photoelectric detectors. *Soviet Journal of Quantum Electronics*, 10(9):1112, 1980.
- [31] Tommaso Lunghi, Boris Korzh, Bruno Sanguinetti, and Hugo Zbinden. Absolute calibration of fiber-coupled single-photon detector. *Opt. Express*, 22(15):18078–18092, Jul 2014.
- [32] W. P. Grice and I. A. Walmsley. Spectral information and distinguishability in type-ii down-conversion with a broadband pump. *Phys. Rev. A*, 56:1627–1634, Aug 1997.
- [33] Nicolás Quesada and JE Sipe. Time-ordering effects in the generation of entangled photons using nonlinear optical processes. *Physical review letters*, 114(9):093903, 2015.
- [34] M.D. Vidrighin. *Quantum Optical Measurements for Practical Estimation and Information Thermodynamics*. PhD thesis, Imperial College London, 2016.
- [35] Fujio Shimizu. Frequency broadening in liquids by a short light pulse. *Phys. Rev. Lett.*, 19:1097–1100, Nov 1967.
- [36] J. H. Eberly. Schmidt analysis of pure-state entanglement. *Laser Physics*, 16(6):921–926, Jun 2006.
- [37] T Sh Iskhakov, K Yu Spasibko, M V Chekhova, and G Leuchs. Macroscopic hong-ou mandel interference. *New Journal of Physics*, 15(9):093036, 2013.
- [38] I V Dyakonov, P R Sharapova, T Sh Iskhakov, and G Leuchs. Direct schmidt number measurement of high-gain parametric down conversion. *Laser Physics Letters*, 12(6):065202, 2015.
- [39] P.J. Mosley. *Generation of heralded single photons in pure quantum states*. PhD thesis, University of Oxford, 2007.
- [40] M.M. Fejer, G.A. Magel, D.H. Jundt, and R.L. Byer. Quasi-phase-matched second harmonic generation: tuning and tolerances. *Journal of quantum electronics*, 28(11), 1992.
- [41] Investigation of optical inhomogeneity of mgo:ppln crystals for frequency doubling of 1560nm laser. *Optics Communications*, 326:114 – 120, 2014.
- [42] U. Fano. Effects of configuration interaction on intensities and phase shifts. *Phys. Rev.*, 124:1866–1878, Dec 1961.
- [43] Robert W Boyd. *Nonlinear optics*. Elsevier, 2003.

Appendix A: Quantum and classical input-output relations

We can exactly find the transformation that describes the Heisenberg picture evolution of the creation/annihilation operators by looking at how it transforms the classical coherent amplitudes of a seed field. A broadband coherent seed in the signal (idler) mode can be

described as a displaced vacuum, which in the Heisenberg picture can be represented by splitting a creation operation in terms of its mean value $\alpha_{s,i}$ and its fluctuations $\delta a_{s,i}$

$$a_{s(i)}^{(\text{in})}(\omega) = \alpha_{s(i)}(\omega) + \delta a_{s(i)}(\omega). \quad (\text{A1})$$

The seed field is evolved following equation 1:

$$a_s^{(\text{out})}(\omega) = \int d\omega' U^{s,s}(\omega, \omega') [\delta a_s(\omega') + \alpha_s(\omega')] + \int d\omega' U^{s,i}(\omega, \omega') [\delta a_i^\dagger(\omega') + \alpha_i(\omega')] \quad (\text{A2})$$

A spectrally resolved power measurement of the signal fields yields:

$$P_s(\omega) \propto \langle [a_s^{(\text{out})}(\omega)]^\dagger a_s^{(\text{out})}(\omega) \rangle = \left| \int d\omega d\omega' U^{s,s}(\omega, \omega') \alpha_s(\omega') \right|^2 + \left| \int d\omega d\omega' U^{s,i}(\omega, \omega') \alpha_i(\omega') \right|^2 + \left| \int d\omega d\omega' U^{s,i}(\omega, \omega') \right|^2, \quad (\text{A3})$$

and a similar equation for the idler power. We identify three contributions to the PSD: the first, involving the self-mode TFs, represents the seed power and cascaded DFG. The second, involving the cross-mode TF, represents stimulated emission (and higher order cascaded DFG terms). The third term represents spontaneous emission. This last term is negligible for strong enough seed fields.

Appendix B: Second order perturbative expansion of PDC

Here we perturbatively solve the PDC equations of motion (6a,6b) up to second order in the PDC gain. We show that, while the term linear in γ_{PDC} yields the usual joint spectral amplitude, the second order term yields a broadband pedestal in the same-mode transfer function. This illustrates our simple physical picture: the same mode emission is caused by a cascaded process where a broadband signal (idler) photon stimulated by the narrowband idler (signal) seed subsequently stimulates broadband emission in the idler (signal) mode. Our fundamental integral equations are

$$a_s(z, \omega) = a_s(z_0, \omega) e^{i\Delta k_s(\omega)(z-z_0)} + \frac{i\gamma_{\text{PDC}}}{\sqrt{2\pi}} \int_{z_0}^z dz' g(z') e^{i\Delta k_s(\omega)(z-z')} \int d\omega' \beta_p(z', \omega + \omega') a_i^\dagger(z', \omega'), \quad (\text{B1})$$

$$a_i(z, \omega) = a_i(z_0, \omega) e^{i\Delta k_i(\omega)(z-z_0)} + \frac{i\gamma_{\text{PDC}}}{\sqrt{2\pi}} \int_{z_0}^z dz' g(z') e^{i\Delta k_i(\omega)(z-z')} \int d\omega' \beta_p(z', \omega + \omega') a_s^\dagger(z', \omega'). \quad (\text{B2})$$

The equations above are clearly formal solutions of equations (6a,6b). Taking the adjoints and substituting into (B1) we have

$$a_s(z, \omega) = a_s(z_0, \omega) e^{i\Delta k_s(\omega)(z-z_0)} + \frac{i\gamma_{\text{PDC}}}{\sqrt{2\pi}} \int_{z_0}^z dz' g(z') e^{i\Delta k_s(\omega)(z-z')} \int d\omega' \beta_p(z', \omega + \omega') e^{-i\Delta k_i(\omega')(z'-z_0)} a_i^\dagger(z_0, \omega') \quad (\text{B3})$$

$$+ \frac{\gamma_{\text{PDC}}^2}{2\pi} \int_{z_0}^z dz' g(z') \int_{z_0}^{z'} dz'' g^*(z'') e^{i\Delta k_s(\omega)(z-z')} \int \int d\omega' d\omega'' \beta_p(z', \omega + \omega') e^{-i\Delta k_i(\omega')(z'-z'')} \beta_p^*(z'', \omega' + \omega'') a_s(z'', \omega''),$$

and a similar equal for the evolution of $a_i(z, \omega)$ obtained by letting $s \leftrightarrow i$ in the last equation. In what follows we only write equations for the signal but it is understood that a similar equation follows for the idler using the rule written in the last sentence.

These expressions are still exact. Beginning an iteration and looking at a final $z = z_1$ we have

$$\begin{aligned}
a_s(z_1, \omega) = & a_s(z_0, \omega) e^{i\Delta k_s(\omega)(z_1 - z_0)} + \frac{i\gamma_{\text{PDC}}}{\sqrt{2\pi}} \int_{z_0}^{z_1} dz' g(z') e^{i\Delta k_s(\omega)(z_1 - z')} \int d\omega' \beta_p(z', \omega + \omega') e^{-i\Delta k_i(\omega')(z' - z_0)} a_i^\dagger(z_0, \omega') \\
& + \frac{\gamma_{\text{PDC}}^2}{2\pi} \int_{z_0}^{z_1} dz' g(z') \int_{z_0}^{z'} dz'' g^*(z'') e^{i\Delta k_s(\omega)(z_1 - z')} \\
& \times \int d\omega' d\omega'' \beta_p(z', \omega + \omega') e^{-i\Delta k_i(\omega')(z' - z'')} \beta_p^*(z'', \omega' + \omega'') e^{i\Delta k_s(\omega'')(z'' - z_0)} a_s(z_0, \omega''). \tag{B4}
\end{aligned}$$

Then writing

$$\begin{aligned}
a_s^{(\text{out})}(\omega) &= \int d\omega'' U^{s,s}(\omega, \omega'') a_s^{(\text{in})}(\omega'') + \int d\omega' U^{s,i}(\omega, \omega') a_i^{\dagger(\text{in})}(\omega'), \\
a_i^{(\text{out})}(\omega) &= \int d\omega'' U^{i,i}(\omega, \omega'') a_i^{(\text{in})}(\omega'') + \int d\omega' U^{i,s}(\omega, \omega') a_s^{\dagger(\text{in})}(\omega'), \\
a_x^{(\text{in})}(\omega) &= e^{-i\Delta k_x(\omega)z_0} a_x(z_0, \omega), \quad a_x^{(\text{out})}(\omega) = e^{-i\Delta k_x(\omega)z_0} a_x(z_1, \omega)
\end{aligned}$$

we have

$$U^{s,s}(\omega, \omega'') = \delta(\omega - \omega'') \tag{B5}$$

$$+ \frac{\gamma_{\text{PDC}}^2}{2\pi} \int_{z_0}^{z_1} dz' g(z') \int_{z_0}^{z'} dz'' g^*(z'') e^{-i\Delta k_s(\omega)z'} \int d\omega' \beta_p(z', \omega + \omega') e^{-i\Delta k_i(\omega')(z' - z'')} \beta_p^*(z'', \omega'' + \omega') e^{i\Delta k_s(\omega'')z''},$$

$$U^{s,i}(\omega, \omega') = \frac{i\gamma_{\text{PDC}}}{\sqrt{2\pi}} \int_{z_0}^{z_1} dz' e^{-i\Delta k_s(\omega)z'} g(z') \beta_p(z', \omega + \omega') e^{-i\Delta k_i(\omega')z'}. \tag{B6}$$

The first-order perturbative result in $U^{s,i}$ in the last set of equations describes how a field in the idler (signal) mode stimulates the generation of a field in the signal (idler) mode, and is often employed in the context of photo-pair generation, where the first order approximation of $U^{s,i(i,s)}(\omega, \omega')$ is the joint spectrum of SPDC photon pairs. This can be written in a more elegant form by introducing the phase-matching function (PMF)

$$\Phi(\Delta k(\omega, \omega')) = \int_{z_0}^{z_1} \frac{dz}{\sqrt{2\pi}} g(z) e^{-i\Delta k(\omega, \omega')z}, \tag{B7}$$

$$\Delta k(\omega, \omega') = \Delta k_s(\omega) + \Delta k_i(\omega') \tag{B8}$$

$$= (\Delta\beta_s)(\omega - \bar{\omega}_s) + (\Delta\beta_i)(\omega' - \bar{\omega}_i), \tag{B9}$$

$$\Delta\beta_x = 1/v_x - 1/v_p, \tag{B10}$$

and recalling that in the low gain regime the spectral content of the pump is not changed allowing us to write

$$\beta_p(z, \omega + \omega') = \sqrt{\frac{E_p}{\sigma}} F\left(\frac{\omega - \bar{\omega}_s + \omega' - \bar{\omega}_i}{\sigma}\right), \tag{B11}$$

where $F(x)$ is the \mathcal{L}^2 normalized pump shape (i.e. $\int dx |F(x)|^2 = 1$) and we used the fact that $\bar{\omega}_p = \bar{\omega}_s + \bar{\omega}_i$. With these definitions we finally write

$$U^{s,i}(\omega, \omega') = i\gamma_{\text{PDC}} \sqrt{\frac{E_p}{\sigma}} F\left(\frac{\omega + \omega' - \bar{\omega}_p}{\sigma}\right) \Phi(\Delta k(\omega, \omega')). \tag{B12}$$

Note that if, for example, $g(z)$ is a top hat function of length L centered at the origin then

$$\Phi(\Delta k(\omega, \omega')) = \frac{L}{\sqrt{2\pi}} \text{sinc}(\Delta k(\omega, \omega')L/2). \tag{B13}$$

The mean number of spontaneously generated signal (idler) photons per pump pulse is thus

$$\begin{aligned}
\langle n_{s(i)} \rangle &= \int d\omega \langle a_s^\dagger(\omega) a_s(\omega) \rangle = \int d\omega d\omega' |U^{s,i}(\omega, \omega')|^2 \\
&= \frac{\gamma_{\text{PDC}}^2 E_p \ell}{\left| \frac{1}{v_s} - \frac{1}{v_i} \right|}, \tag{B14}
\end{aligned}$$

where $\ell = \int_{\ell_{\min}}^{\ell_{\max}} dz |g(z)|^2$ is the effective length of the crystal. Note that a $g(z)$ with a top hat shape of length L will have precisely that $\ell = L$.

In a stimulated experiment where the idler (signal) is seeded, broadband DFG will be generated in the conjugate mode (Appendix A) with a total intensity $I_{s(i)} \propto \int d\omega d\omega' |U^{s,i(i,s)}(\omega, \omega')|^2 = \langle n_{s(i)} \rangle$.

The second order term which appears in $U^{s,s}(\omega, \omega')$ and $U^{i,i}(\omega, \omega')$ generates a broadband contribution in the seeded mode with amplitude proportional to the square of the PDC gain.

Under certain circumstances it is possible to evaluate this term analytically. For this we will assume a Gaussian

nonlinearity profile and pump profile

$$g(z) = \frac{1}{\sqrt[4]{\pi\gamma/2}} e^{-\frac{z^2}{\gamma\ell^2}}, \quad F(x) = \frac{1}{\sqrt[4]{\pi}} e^{-\frac{x^2}{2}}, \quad (\text{B15})$$

where $\gamma \approx 0.193$ is chosen so that the PMF associated with this nonlinearity profile has the same full width at half maximum of the one associated with a top hat profile. Under these approximations, letting $z_0 \rightarrow -\infty$ and $z_1 \rightarrow +\infty$ one can write the intermode transfer function as a double Gaussian

$$U^{s,i}(\omega, \omega') = i\gamma_{\text{PDC}}\ell \sqrt{\frac{E_p}{\pi\sigma}} \sqrt{\gamma/2} \exp(-\mathbf{vMv}^T), \quad (\text{B16})$$

$$\mathbf{v} = (\omega - \bar{\omega}_s, \omega' - \bar{\omega}_i), \quad (\text{B17})$$

$$\mathbf{M} = \begin{pmatrix} \mu_s^2 & \mu^2 \\ \mu^2 & \mu_i^2 \end{pmatrix}, \quad (\text{B18})$$

$$\mu_{s,i}^2 = \frac{1}{4}\ell^2\gamma\Delta\beta_{s,i}^2 + \frac{1}{2\sigma^2}, \quad (\text{B19})$$

$$\mu^2 = \frac{1}{4}\gamma\Delta\beta_i\Delta\beta_s\ell^2 + \frac{1}{2\sigma^2}. \quad (\text{B20})$$

Similarly, one can write a simple analytical expression for the second-order intramode transfer function

$$U^{s,s}(\omega, \omega'') = \delta(\omega - \omega'') + U_b^{s,s}(\omega, \omega''), \quad (\text{B21a})$$

$$U_b^{s,s}(\omega, \omega'') = \frac{\gamma_{\text{PDC}}^2 E_p \ell^2 \sqrt{\gamma}}{\sqrt{\pi}\sigma\mu_i} e^{-x_-^2 - x_+^2} (1 + i \operatorname{erfi}(x_+)), \quad (\text{B21b})$$

$$x_+ = \frac{\frac{\sqrt{\gamma}\ell}{2} \left(\frac{1}{v_s} - \frac{1}{v_i} \right)}{2\sigma\mu_i} (\omega + \omega'' - 2\bar{\omega}_s), \quad (\text{B21c})$$

$$x_- = \frac{\mu_s}{\sqrt{2}} (\omega - \omega''), \quad (\text{B21d})$$

and $\operatorname{erfi}(x) = \operatorname{erf}(ix)/i$ is the imaginary error function, which is an odd function of its argument. Because of this the phase of $U_b^{s,s}(\omega, \omega'')$ has a jump when crossing the line $\omega + \omega'' - 2\bar{\omega}_s = 0$. This will become a useful observation when we compare the form of the transfer function of the cascaded (second order) $\chi^{(2)}$ process, which as just mentioned as a phase jump, and the pure $\chi^{(3)}$ process which does not. Finally, note that an analogous expression for the intramode transfer function $U_b^{i,i}(\omega, \omega'')$ can be obtained by letting $i \leftrightarrow s$ in Eq. (B21).

Appendix C: Experimental setup details

The nonlinear crystal in our experiment is an 8mm ppKTP chip manufactured by ADVR, made from a z-cut wafer, with a set of waveguides written using a proton exchange process. The waveguides are roughly $4\mu\text{m} \times 4\mu\text{m}$ in cross section. The chip output is AR coated for 1550 nm. We pump the source with a pulsed Ti:Sapphire laser (Coherent Chameleon) with central wavelength 783 nm

and 8nm bandwidth, which we filter using two bandpass thin-film filters (Semrock LL01-785-12.5) to a bandwidth of 1.9 nm. The periodic poling has a spatial period of $104\mu\text{m}$, which leads to quasi-phase matching for signal and idler around 1560 nm. Using an ordinarily polarized pump (H polarization), we obtain a signal (H polarization) and idler (V polarization) beams with respective central wavelengths of 1563 nm and 1569 nm.

The phase-matching of the type-II PDC process has been engineered to obtain signal and idler fields at telecom wavelengths with an almost separable joint spectrum. In the weak squeezing regime, where we may approximate that only single photon pairs are produced, the joint spectrum of a PDC source can be expressed as a product of two factors: a pump function and a phase matching function [32]. As illustrated in Figure 10, the pump function, related to energy conservation, introduces anti-correlation of the frequencies of photons generated in the PDC process. The nature of the phase matching function, related to momentum conservation, depends on the dispersion relation of the guided modes. In a medium with normal dispersion, both signal and idler commonly have higher group velocity than the pump, resulting in frequency anti-correlations [39]. In the waveguided ppKTP, due to the birefringence of the material the group velocity of a pump field at 780 nm in the ordinary polarization falls in between the group velocities of the signal and idler fields centered around 1560 nm in orthogonal polarizations. This results in a phase-matching function with positive frequency correlations [2]. The combined effect of these two factors with the correct balance of pump and phase matching bandwidths, as illustrated in Figure 10, can produce an almost separable joint spectrum.

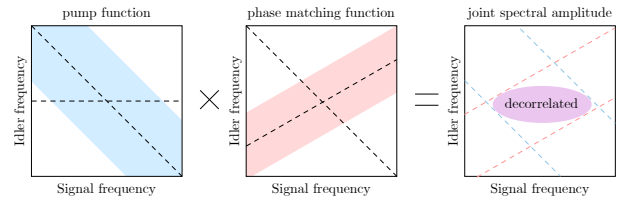


FIG. 10: The product of a pump function (energy conservation) and a phase-matching function (momentum conservation) can yield a separable joint spectrum

To measure the direct and cascaded DFG signals we seed one of the downconverted fields with a continuous wave (CW) laser and measure the generated stimulated emission using an optical spectrum analyzer (OSA). For the seed field we use a Yenista Tunics T100S-HP CW fiber laser with wavelength tunable between 1500nm and 1680nm. The laser has a very high spontaneous noise suppression, over 100 dB over a bandwidth of 1 nm. After polarization filtering using birefringent waveplates and a Glan-Taylor polarizer, we record spectra of the generated light using a Yokogawa AQ6370D optical spectrum analyzer (OSA). The OSA has a high dynamic range of 78

dB over 1nm, allowing us to distinguish the weak broadband cascaded DFG signal ($<1\text{nW}$) from the narrowband seed ($\approx 600\mu\text{W}$). While the linewidth of the seed laser is many orders of magnitude smaller than the broadband cascaded DFG emission, the finite resolution of the OSA (0.2 nm) broadens the width of the narrowband component of the spectra, hindering the retrieval of the broadband pedestal. To remove the CW seed from the data we first subtract a background trace from it, where we send the seed beam but not the pump through the crystal. Fluctuations of the seed power between the moment when the data and the background are measured lead to an imperfect extinction of the narrowband component. We eliminate this CW remnant by masking the frequency range occupied by it and interpolating the remaining spectrum, as illustrated in Figure 11.

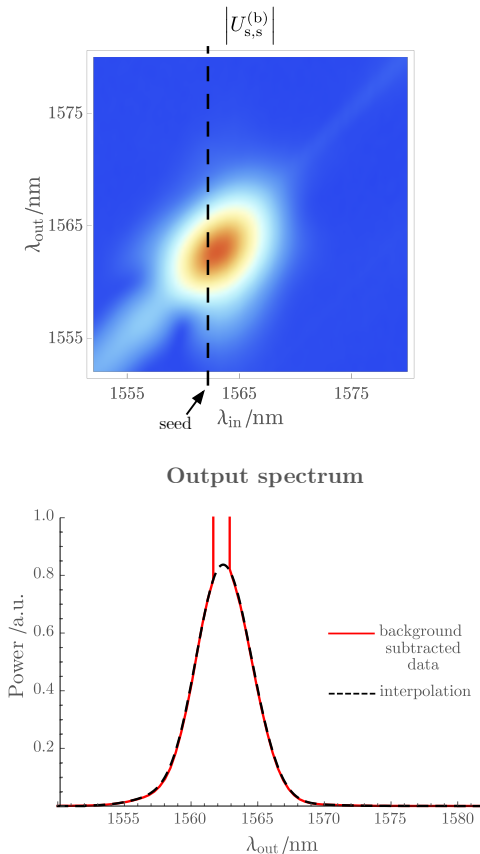


FIG. 11: a). Reconstruction of the stimulated emission spectrum as a function of seeding wavelength, measured in the seed polarization; color indicates the absolute value of the field (square root of the measured spectral power density) b). Red – One "slice" of the background subtracted data, showing a noisy measurement around the seed wavelength, where the OSA detector is blinded by the seed; black – reconstructed spectrum obtained by interpolating over the noisy region.

Appendix D: Identifying the EOM parameters

In this Appendix, we describe in detail how we identify the physical parameters that enter in our theoretical description (6a,6b,7) of the SPDC. We describe how these parameters can be extracted from the TF data mostly in the small gain limit, complemented with some additional measurements.

1. Pump spectral intensity

The pump spectral amplitude at position z in the crystal, $\beta_p(z, \omega)$, is a complex-valued function. In our experiment, we measure the absolute value of $\beta_p(z = 0, \omega)$ in two ways (see figure 12): First, we perform a direct measurement of the pump spectrum at the chip input using an optical spectrum analyzer (OSA), which provides the squared modulus of the pump spectral amplitude. Second, we confirm this result by extracting the pump spectral density from low gain cross-mode TF measurements.

2. Pump spectral phase

We used an APE LX-Spider (wavelength range between 750 and 900 nm), to characterize the spectral phase of the Ti:Sapphire pump laser, but could not extend that measurement to the filtered pump (1.9 nm bandwidth) because of the limit in the spectral resolution of the apparatus. We characterized the spectral phase added by the filters using a spectral self-interference measurement: the filtered pump is interfered with a sample of the same, unfiltered field, thus revealing their differential spectral phase. The total spectral phase of the pump is obtained by adding the spectral phase of the reference beam, measured using SPIDER, and the phase added by the optical filters, measured through spectral interference.

Let us briefly detail the spectral interference process by which we measure the phase added by the optical filters. The complex spectral amplitude corresponding to the sum of the unfiltered reference, β_{ref} , and filtered pump field, $\beta_p(\omega)$, is

$$\beta_{\text{sum}}(\omega) = \beta_{\text{ref}} + |\beta_p(\omega)| \exp\left(i(\phi(\omega) + \Delta t \omega)\right), \quad (\text{D1})$$

where we are omitting the spatial label in the field amplitudes, implicitly assuming a position before the chip input. We assume that the unfiltered reference is much broader than the filtered pump, such that the former can be treated as a field with a constant spectral density. Without loss of generality, we also take the spectral phase as constant. The phase of the filtered pump is the sum of $\phi(\omega)$, the phase added in the filtering process, and $\Delta t \omega$, representing a temporal delay with respect to the reference field.

The measured PSD is:

$$P(\omega) \propto |\beta_{\text{sum}}(\omega)|^2 \quad (\text{D2})$$

$$= |\beta_{\text{ref}}|^2 + |\beta_{\text{p}}(\omega)|^2 + |\beta_{\text{ref}}||\beta_{\text{p}}(\omega)| \cos(\phi(\omega) - \Delta t \omega),$$

where we recognize that the last term describes spectral fringes with a period of approximately $1/\Delta t$, modulated by the spectral phase added by the optical filters. We assume that the delay between the interfering beams is large, so that the interference fringes that it causes are fast compared with the spectral interference due to the filters' spectral phase. This modulation can be retrieved by keeping only positive frequencies above the bandwidth of the base-band component of $I(\omega)$, which corresponds to the complex signal

$$P_{\text{HF}} \propto |\beta_{\text{ref}}||\beta_{\text{p}}(\omega)| \exp(\Delta t \omega + \phi(\omega)). \quad (\text{D3})$$

The argument of which corresponds to the spectral phase added by the filters, modulo a linear component.

Our SPIDER measurement reveals that the chirp introduced in the unfiltered pump by the power-distribution optics is small, reaching less than 0.1 rad over the filtered pump bandwidth. The spectral phase added by the dielectric filters is the main contribution to the total spectral phase. This measurement agrees with the specifications provided by the supplier of the filters (Semrock). In figure 12 we show the measured magnitude and phase of the pump spectral amplitude.

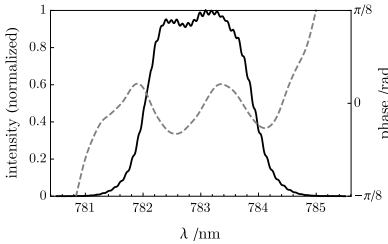


FIG. 12: Magnitude (solid line) and phase (dashed line) of the filtered pump spectral amplitude. The magnitude shown here corresponds to that measured using the OSA, and agrees very well with the pump function of a low gain JSI. The phase shown here corresponds to the addition of the phase of the unfiltered pump measured using SPIDER, and the differential phase of the filtered pump measured through spectral interferometry.

3. Group velocity mismatch

In our model the group velocities of the pump, signal, and idler fields determine the linear propagation of the fields in the crystal. We need the two group velocity mismatch parameters, $\Delta\beta_{s(i)} = 1/v_{s(i)} - 1/v_{\text{p}}$. The phase matching (PM) function (see Appendix B) of a low gain joint spectral amplitude has the simple form

$$\Phi_{\text{PM}}(\Omega_{\text{s}}, \Omega_{\text{i}}) \propto \text{sinc}\left(\frac{L}{2}(\Delta\beta_{\text{s}}\Omega_{\text{s}} + \Delta\beta_{\text{i}}\Omega_{\text{i}})\right), \quad (\text{D4})$$

where L is the crystal length and $\Omega_{s(i)} = \omega_{s(i)} - \bar{\omega}_{s(i)}$ are the detunings from the central phase-matching frequencies. Perfect phase-matching occurs for frequencies $\Omega_{\text{i}} = \Omega_{\text{s}} \tan(\theta_{\text{PM}})$, with $\tan(\theta_{\text{PM}}) = -\Delta\beta_{\text{s}}/\Delta\beta_{\text{i}}$. Rotating to a frequency frame by the phase matching angle, θ_{PM} ,

$$\Omega_{\parallel} = \cos(\theta_{\text{PM}})\Omega_{\text{s}} + \sin(\theta_{\text{PM}})\Omega_{\text{i}}, \quad (\text{D5})$$

$$\Omega_{\perp} = \cos(\theta_{\text{PM}})\Omega_{\text{i}} - \sin(\theta_{\text{PM}})\Omega_{\text{s}}, \quad (\text{D6})$$

the phase-matching function depends only on the perpendicular component:

$$\Phi_{\text{PM}}(\Omega_{\perp}) \propto \text{sinc}\left(\frac{1}{2}\Omega_{\perp} \frac{\Delta\mu}{\cos(\theta_{\text{PM}}) + \sin(\theta_{\text{PM}})}\right), \quad (\text{D7})$$

where we have introduced the quantity $\Delta\mu = L(\Delta\beta_{\text{s}} - \Delta\beta_{\text{i}}) = L(1/v_{\text{s}} - 1/v_{\text{i}})$, which corresponds to the group delay between the signal and idler over the crystal length. This parametrization makes it clear that, in the symmetric group velocity matching case, the phase-matching bandwidth is inversely proportional to the walk-off between the signal and idler pulses in the crystal. We can write the group velocity mismatch parameters, $\Delta\beta_{s(i)}$, in terms of $\Delta\mu$ and θ_{PM} as

$$\Delta\beta_{\text{s}} = \frac{\Delta\mu}{L} \frac{\tan(\theta_{\text{PM}})}{\tan(\theta_{\text{PM}}) + 1}, \quad (\text{D8a})$$

$$\Delta\beta_{\text{i}} = -\frac{\Delta\mu}{L} \frac{1}{\tan(\theta_{\text{PM}}) + 1}. \quad (\text{D8b})$$

To obtain the phase matching angle, θ_{PM} , we reconstruct a broad section of the phase matching function by measuring the cross-mode TF as we scan the pump power and joining the resulting measurements (see Figure 13.a). We found the phase-matching angle $\theta_{\text{PM}} = 59.2^\circ$.

The second parameter, $\Delta\mu$, can be obtained by measuring the spectral interference due to walk-off between pulses in the signal and idler polarizations propagating through the source. We launched broadband light from a very broadband (~ 100 nm) superluminescent light-emitting diode (SLED) in diagonal polarization through the ppKTP wave-guide. The input polarization state can be written as $|D\rangle = (|H\rangle + |V\rangle)/\sqrt{2}$. The output polarization state is then $(e^{i\phi_{\text{H}}} |H\rangle + e^{i\phi_{\text{V}}} |V\rangle)/\sqrt{2}$. Up to first order in the wavelength λ , we have

$$\begin{aligned} \phi_{\text{V}} - \phi_{\text{H}} &= \\ \omega_0 L \left[\left(\frac{n_{\text{V}}(\omega_0) - n_{\text{H}}(\omega_0)}{c} + \frac{1}{v_{\text{i}}} - \frac{1}{v_{\text{s}}} \right) + \left(\frac{1}{v_{\text{s}}} - \frac{1}{v_{\text{i}}} \right) \frac{\lambda}{\lambda_0} \right] \\ &= \text{constant} + \frac{2\pi c}{\lambda_0^2} \Delta\mu \lambda, \end{aligned} \quad (\text{D9})$$

where ω_0 is the central frequency of the signal/idler fields, λ_0 is the corresponding central wavelength in vacuum, and $n_{\text{V/H}}(\omega_0)$ is the refractive index experienced by the vertical/horizontal polarizations of a field at said central wavelength. Thus, when we project the output on

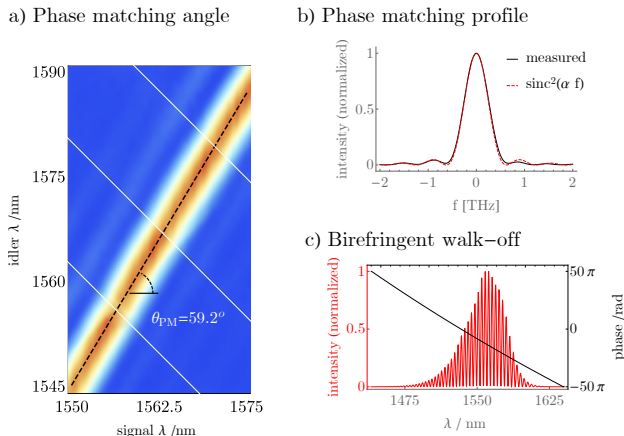


FIG. 13: Group velocity mismatch characterization. a) Measurement of the phase matching angle. Four low gain JSIs with different pump central frequencies are joined to reconstruct a long section of the phase matching function. b) Inference of $\Delta\mu$ by measuring the bandwidth of the phase matching profile. The measured intensity profile (solid black line) is fitted with a sinc^2 function (dashed red line), and the group delay is obtained from equation (D7). c) Direct measurement of $\Delta\mu$ by measuring spectral interference between two orthogonal polarizations of a broadband SLED after traveling through the crystal. The oscillating spectral intensity (red line) is transformed to the Fourier domain and a corresponding spectral phase is obtained (black line), from which the spectral oscillation period is retrieved.

the diagonal polarization, in the output wavelength spectrum we will observe fringes with period $\lambda_0^2/(c\Delta\mu)$. Figure 13.c shows our measurement of these spectral fringes, from which we extract a delay between signal and idler of $\Delta\mu = 2.2$ ps.

As shown in Figure 13.b, we independently infer the value of $\Delta\mu$ by measuring the phase-matching profile of a low gain JSI and fitting it to the function predicted in Equation (D7). While it is known that inhomogeneities in the periodic poling of a nonlinear crystal lead to distortions of the phase-matching profile [40, 41], the good fit of the data to a “sinc” function allows us to assume that the periodic poling in this waveguide does not show a significant inhomogeneity. We must note that this was not the case in other waveguides of the same chip, which yielded phase-matching profiles showing important deviations from a “sinc” function (see Figure 14). The value of the group delay that fits the bandwidth of the measured phase-matching profile is again $\Delta\mu = 2.2$ ps, confirming our previous measurement.

The values of the group velocity mismatch parameters retrieved from Equations (D8a,D8b) together with the results of our measurements, and assuming a crystal of length of $L = 8$ mm, are $\beta_s = 1.7$ ps/cm and $\beta_i = -1.0$ ps/cm.

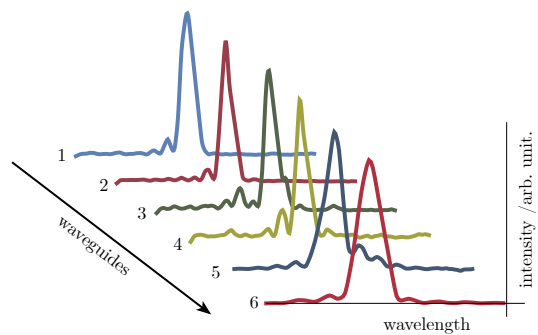


FIG. 14: Phase matching profiles of different waveguides in the same chip. We observe a variability of the shape of the phase-matching profiles which can be caused by periodic poling inhomogeneity.

4. Parametric down-conversion gain

In the low gain regime, where the effect of SPM and XPM can be neglected, and assuming a homogeneous periodic poling, the PDC equations of motion (6a, 6b) are defined solely by $\Delta\beta_s, \Delta\beta_i$ and $\beta_p(z = 0, \omega)$, as well as the PDC coupling strength, γ_{PDC} . Integrating the EOMs allows us to compute the quantity κ , as defined in equation (5), which, as we have explained in Sec IB, is independent of the seeding and detection efficiency, using γ_{PDC} as a free fitting parameter. From the results in Appendix B, one can easily show that κ is linearly proportional to γ_{PDC} in the low gain regime. In the high gain regime, the relation between κ and γ_{PDC} becomes nonlinear, but it remains monotonically increasing. This monotonic dependence allows us to use κ as a robust proxy to derive the PDC coupling strength, γ_{PDC} , from experimental intensity ratios.

In our experimental demonstration, we fit the predictions of our model to the experimental values of κ as a function of pump pulse energy, as illustrated in figure 6. In order to mitigate the effect of measurement noise, we smooth the spectral distributions using a Gaussian kernel with a standard deviation of 0.35 nm before taking their maxima. The best fit parameter was $\gamma_{\text{PDC}} = 28 \text{ W}^{-1/2}/\text{m}^{-1}$.

5. Cross-phase modulation

Cross-phase modulation of the narrowband seed by the broadband pump appears as a spectral broadening of the former. In our seeded measurements, this effect shows as a broadband pedestal surrounding the CW component of the same-mode TFs. According to our simulations of $U_b^{s,s/i,i}(\omega_{\text{out}}, \omega_{\text{in}})$, the amplitude is constant along a contour where $\omega_{\text{in}} + \omega_{\text{out}}$ is constant, and its magnitude is proportional to the power of the pump. As mentioned in previous appendices (e.g Appendix B), the same-mode TFs contain another broadband component

due to cascaded PDC. Our simulations show that the cascaded PDC amplitude scales linearly with the pump power and it exhibits a π phase jump around the central phase-matching wavelength (this is also readily seen by examining the analytical result in Eq. (B21)). Due to this non-trivial spectral phase, the XPM and PDC contributions interfere either constructively or destructively at different frequencies, resulting in an emission spectrum shaped like a Fano resonance [42], as illustrated in figure 15. The asymmetry of this spectrum allows us to accurately estimate the XPM coupling strength in relation to the PDC coupling strength. In Figure 4 we use diagonal cuts of the same-mode TFs at the lowest power (in order to avoid other nonlinear phenomena) and find the XPM interaction strength $\gamma_{\text{XPM},s(i)}$ that best fits their asymmetric “tails”. The best fit parameters were $\gamma_{\text{XPM},s} = 0.16 \text{ W}^{-1}\text{m}^{-1}$ and $\gamma_{\text{XPM},i} = 0.06 \text{ W}^{-1}\text{m}^{-1}$.

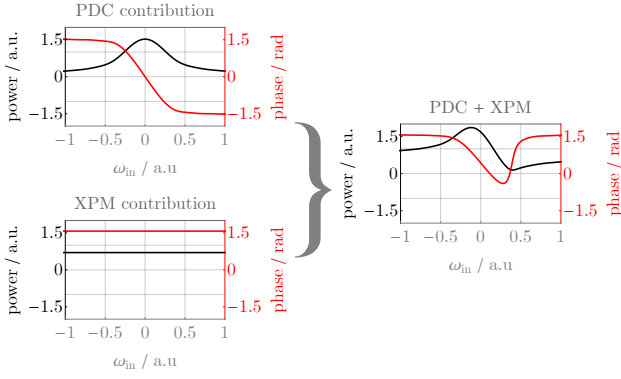


FIG. 15: Asymmetric magnitude of the TF “cut” $U_{(b)}^{s,s}(\omega, \omega)$ due to interference between PDC and XPM. Left, top – Simulated cut with only PDC. Left, bottom – Simulated cut with only XPM. Right – Simulated cut with PDC and XPM.

6. Self-phase modulation of the pump

The effect of SPM of the pump is visible in the high gain regime: the cross-mode TFs show a clear broadening, as well as splitting of the pump function. Also, the same-mode TFs lose their symmetry, which is consistent with a chirped pump, as illustrated in figure 5.

Assuming that dispersion of the pump is negligible, its evolution along the waveguide is given by the differential equation (7). Having measured $\beta_p(z=0, \omega)$, the SPM interaction strength γ_{SPM} is the only fitting parameter left, which determines the evolution of the pump spectral amplitude along the waveguide. To obtain the value of γ_{SPM} , we take the complete signal/idler EOMs (6a,6b), with all the other parameters fitted using the low gain regime measurements described above, and find the value of the SPM interaction strength that best fits the high gain TFs according to the error met-

ric defined in Equation (11). The best fit parameter was $\gamma_{\text{SPM}} = 0.56 \text{ W}^{-1} \text{ m}^{-1}$.

Appendix E: Asymmetry in the cross-phase modulation coefficients

In this appendix we provide an analysis of the way in which waves propagating in a material can experience different nonlinear effects because of their polarization relative to a strong pump. Suppose we have a pump wave with central frequency $\bar{\omega}_p$ and a signal wave with central frequency $\bar{\omega}_s$ polarized in the same direction, say the y direction. Then the polarization term responsible for the XPM will be [43]

$$P_y(\bar{\omega}_s) = \epsilon_0 \chi_{yyy}^{(3)} E_y(\bar{\omega}_s) E_y(\bar{\omega}_p) E_y(-\bar{\omega}_p) + \dots \quad (\text{E1})$$

where \dots are terms obtained by permuting the different fields appearing in the first term. The fields associated with the three frequencies ($\bar{\omega}_s, \bar{\omega}_p, -\bar{\omega}_p$) can be combined in any order, giving $3! = 6$ different terms. So in all we would have

$$P_y(\bar{\omega}_s) = 6\epsilon_0 \chi_{yyy}^{(3)} E_y(\bar{\omega}_s) E_y(\bar{\omega}_p) E_y(-\bar{\omega}_p). \quad (\text{E2})$$

Now suppose the pump is in the y direction but the idler is in the x direction. Then one of the terms contributing to the cross-phase modulation would be

$$P_x(\bar{\omega}_i) = \epsilon_0 \chi_{xxy}^{(3)} E_x(\bar{\omega}_i) E_y(\bar{\omega}_p) E_y(-\bar{\omega}_p) + \dots \quad (\text{E3})$$

For this particular $\chi^{(3)}$ component we could put the fields at $\bar{\omega}_p$ and $-\bar{\omega}_p$ in other orders, ($2!$ permutations) so from this particular component we would expect

$$P_x(\bar{\omega}_i) = 2\epsilon_0 \chi_{xxy}^{(3)} E_x(\bar{\omega}_i) E_y(\bar{\omega}_p) E_y(-\bar{\omega}_p). \quad (\text{E4})$$

However, there will be other tensor components involving x 's and y 's. In particular we can expect a $\chi_{xyy}^{(3)}$ and a $\chi_{xyxy}^{(3)}$. In each one of these there will be two permutations of the fields at $\bar{\omega}_p$ and $-\bar{\omega}_p$ that share the same Cartesian component, so in all

$$P_x(\bar{\omega}_i) = 2\epsilon_0 \chi_{xxy}^{(3)} E_x(\bar{\omega}_i) E_y(\bar{\omega}_p) E_y(-\bar{\omega}_p) \quad (\text{E5})$$

$$+ 2\epsilon_0 \chi_{xyy}^{(3)} E_y(\bar{\omega}_p) E_y(-\bar{\omega}_p) E_x(\bar{\omega}_i) \quad (\text{E6})$$

$$+ 2\epsilon_0 \chi_{xyxy}^{(3)} E_y(\bar{\omega}_p) E_x(\bar{\omega}_i) E_y(-\bar{\omega}_p) \quad (\text{E7})$$

$$= 2\epsilon_0 (\chi_{xxy}^{(3)} + \chi_{xyy}^{(3)} + \chi_{xyxy}^{(3)}) E_x(\bar{\omega}_i) E_y(\bar{\omega}_p) E_y(-\bar{\omega}_p). \quad (\text{E8})$$

That is for different polarizations. For the same polarization we have (E2). So

$$P_y(\bar{\omega}_s) = 6\epsilon_0 \chi_{yyy}^{(3)} E_y(\bar{\omega}_s) E_y(\bar{\omega}_p) E_y(-\bar{\omega}_p) \quad (\text{same pol.}) \quad (\text{E9})$$

$$P_x(\bar{\omega}_s) = 2\epsilon_0 (\chi_{xxy}^{(3)} + \chi_{xyy}^{(3)} + \chi_{xyxy}^{(3)}) \times \quad (\text{E10})$$

$$E_x(\bar{\omega}_s) E_y(\bar{\omega}_p) E_y(-\bar{\omega}_p) \quad (\text{diff. pol.}) \quad (\text{E11})$$

If one assumes the following symmetry in the third order susceptibility (satisfied for instance by an isotropic medium)

$$\chi_{yyyy}^{(3)} = \chi_{xxyy}^{(3)} + \chi_{xyyx}^{(3)} + \chi_{xyxy}^{(3)}, \quad (\text{E12})$$

so

$$P_y(\bar{\omega}_s) = 6\epsilon_0(\chi_{xxyy}^{(3)} + \chi_{xyyx}^{(3)} + \chi_{xyxy}^{(3)}) \quad (\text{E13})$$

$$\times E_y(\bar{\omega}_s)E_y(\bar{\omega}_p)E_y(-\bar{\omega}_p) \quad (\text{same pol.}) \quad (\text{E14})$$

$$P_x(\bar{\omega}_i) = 2\epsilon_0(\chi_{xxyy}^{(3)} + \chi_{xyyx}^{(3)} + \chi_{xyxy}^{(3)}) \quad (\text{E15})$$

$$E_x(\bar{\omega}_i)E_y(\bar{\omega}_p)E_y(-\bar{\omega}_p) \quad (\text{diff. pol.}), \quad (\text{E16})$$

differing precisely a factor of 3. To the best of our knowledge, the tensor components of the third order nonlinear susceptibility of ppKTP have not been reported in the literature; however, this simple calculation provides a plausible argument for the approximate factor of 3 found between the different cross-phase modulation constants of the signal and idler fields.